Scaffold-enforced Nanoscale Crystalline Order Supersedes Interfacial Interactions in Driving $CsPbI_3$ Perovskite Phase Stability

*Arkita Chakrabarti[1], Benjamin M. Lefler[2†], Aaron T. Fafarman[*1]*

1. Department of Chemical and Biological Engineering, Drexel University, 3141 Chestnut St, Philadelphia, PA, United States, 19104.

2. Department of Material Science and Engineering, Drexel University, 3101 Market St, Philadelphia, PA, United States, 19104.

KEYWORDS: All-inorganic lead halide perovskites, Nanoconfinement, Strain engineering, Phase transition thermodynamics, Self-assembled monolayers, Nanoscaffold composites

ABSTRACT: The equilibrium phase of cesium lead iodide ($CsPbI_3$) is a high density, low symmetry, yellow crystalline solid below 320˚C, above which it transitions to the optoelectronically functional, black, perovskite phase. Several reports have achieved lowered phase transition temperature and increased metastability of perovskite-phase $CsPbI_3$, and attributed the effect variably to reduced size, surface-induced strain and/or external additives. While theory supports that both reduced size and substrate-induced strain can tilt the competition between surface and bulk energies to favor the perovskite phase, there has not been a study of the relative

influence of size and interfacial interactions on this dynamic. In this study, we selectively varied crystalline domain size by embedding $CsPbI_3$ in open nanoporous titania scaffolds composed of particles ranging from 20-200nm and measured the influence on phase transition behavior. We modified the surface of the scaffold using polar, ionizable and non-polar silane self-assembled monolayers (SAMs) to systematically test the extent to which the chemical identity of the interface impacts the surface energy contribution to the phase stability in the perovskite-scaffold composite. While structural and functional consequences were observed for different interfacial chemistries, there was no significant influence on phase equilibrium, and the disruption of long-range crystalline order alone was found to be sufficient to depress the phase transition temperature by more than 250 °C compared to bulk.

Introduction

Over the last several years, the all-inorganic perovskite-phase cesium lead iodide ($CsPbI_3$) has demonstrated increasing promise as an optoelectronic material, especially for photovoltaic applications.[1] Having achieved 19% power conversion efficiency[2], it makes an excellent choice for the absorber layer owing to its compositional stability under environmental stresses, high absorptivity, suitable band gap (1.73 eV) and high charge carrier lifetime. Despite being compositionally robust, the perovskite phase of $CsPbI_3$ suffers from structural instability under ambient conditions: the functional, cubic, black α-phase is the thermodynamically favored polymorph only at temperatures above 320˚C.[3–5] If cooled under controlled conditions, it undergoes a series of octahedral tilts to form distorted cubic, black, metastable, yet functional, β and ɣ phases, until it completely transforms to the non-functional, orthorhombic, yellow δ-phase at room temperature.[6–8] The α, β and ɣ polymorphs are collectively known as the 'perovskite' or simply, 'black' phases.

Stabilization of the functional black phases at lower temperatures has been achieved through incorporation of small-molecule additives[1,9–14], synthesis in the colloidal nanocrystal phase[15–18], confinement within a nanostructured scaffold[19–22], stoichiometric tuning[23] and alloying[24]. Universal to these approaches is the introduction of a barrier, either chemical (additives; colloidal growth) or physical (scaffolds), that limits the perovskite crystal domain size to the order of 10^0-10^2 nm. Recent comprehensive reviews are available.[25,26]

Nanodimensionality has been long known to favor polymorphs of lower density and higher symmetry in crystals whose bonding comprises a mix of ionic and covalent character,[27,28] such as perovskites. A general model for this phenomenon is that truncating a crystal reduces the long range electrostatic attraction, resulting in imbalance between attractive and repulsive forces, thereby driving lattice expansion[27,29], and favoring low density phases. Density Functional Theory (DFT) should be capable of quantitatively predicting the relative stability of different phases as a function of reduced crystal dimensions. To do so, formation energies (energy per formula unit) for each phase, i, ($E_{nano,\,i}$), must be calculated from the sum of the bulk crystal formation ($E_{bulk,i}$) and a term proportional to the surface energy at the boundary of each nanodomain ($E_{surf,i}$). Specifically, for a cube shaped nanocrystal of length, d, and volume per formula unit, V, the nanocrystal formation energy (per formula unit) is given by:

$$E_{nano,\mathrm{i}} = E_{bulk,i} + \frac{E_{surf,i} \cdot 6d^2}{d^3/_V}$$

(where $d^3/_V$ normalizes the surface energy to the number of formula units).[30] The relative stability of a nanocube in the black phase can therefore be calculated as:

$$\Delta E_{nano} = \Delta E_{bulk} + \left(\frac{6V}{d}\right)\Delta E_{surf},$$

where ΔE represents the energy of a black phase, minus that of the yellow. Multiple DFT studies have calculated these quantities and found that although ΔE_{bulk} favors the non-perovskite phase, ΔE_{surf} is less *un*favorable for the black phases; therefore, they predict a thermodynamically favored black phase when the cube is sufficiently small. However, the value of d predicted to confer thermodynamic stability varies over quite a large range, from 5.6 to ~100 nm.[13,30] Examples of spontaneous formation of the perovskite phase of $CsPbI_3$ at room temperature are limited to colloidal nanocrystals with dimensions below 10 nm, in apparent agreement with the more restrictive lower limit.[17,18] Examples of colloidal $CsPbI_3$ do not range significantly larger in size, so experimental tests of the more permissive, 100 nm, predicted limit must be sought for in polycrystalline thin films and scaffold-limited crystals. In these systems, broadening our consideration to slightly elevated temperature, crystal domains as large as 100 nm have been observed to spontaneously adopt the perovskite phase at temperatures as low as 60°C.[23] Despite the breadth of the range of d values, even the more permissive limit does not account for the observed perovskite-phase stability in scaffold-confined $CsPbI_3$ with confinement dimensions as large as 250 nm.[21]

Persistent challenges remain in refining the theory to accurately reflect experimental observation. Is an experimentally observed phase at equilibrium or present in a metastable state? What, if any influence can be attributed to specific interfacial contributions to ΔE_{surf} from the crystal's surroundings, such as interfacial tension and substrate-induced strain? The theories cited above calculate ΔE_{surf} considering an interface with vacuum, while nanostructuring experiments universally involve an interface, which may consist of neighboring crystal domains, impurity inclusions (e.g., surfactants) or a scaffold wall. Hypothetically, for scaffold-supported nanostructures, ΔE_{surf} could depend strongly on the composition of the scaffold surface. For

example, it is known that on unstructured (planar) substrates that the extrinsic interfacial forces, specifically substrate-induced strain, can significantly alter the phase equilibrium[6]. A more favorable ΔE_{surf} has similarly been evoked to account for enhanced stability imparted to colloidal nanocrystals by certain surface ligands.[10,31]

In this work, we take a highly practical approach to nanostructuring: $CsPbI_3$ is coated on porous TiO_2 nanoparticle scaffolds composed of different particle sizes, thereby limiting the long-range crystal order to a size determined by the typical pore size of the scaffold. Typical pore sizes of such scaffolds are slightly smaller than the constituent particles.[32] The TiO_2 scaffold employed is broadly relevant, as it is a ubiquitous electron transport layer in many standard optoelectronic device configurations. In comparison to unstructured films, we differentiate between a metastable perovskite phase that occurs due to the initial nucleation of nanometer sized crystallites that are transitory as opposed to a durably stable perovskite phase made possible when the pore size of the scaffold is significantly below 100 nm. To answer whether the chemical identity of the interface is critical, we systematically varied ΔE_{surf} by functionalizing the scaffold surface with polar, ionizable and non-polar silane self-assembled monolayers (SAMs) and assessed the influence on both stability and photophysics. In this manner, we are able to separately ascertain how the range of the nanocrystalline order and the chemical identity of the interface influence phase-change thermodynamics and atomic and electronic structure.

Experimental Methods

Materials: Cesium iodide 99.99%, Lead iodide 99.99% (TCI America), anhydrous N-methyl-2-pyrrolidone (Acros Organics), Titania paste (Reflector & Transparent) (Sigma Aldrich), 3-aminopropyl trimethoxysilane (Alfa Aesar), 3-cyanopropyl trichlorosilane (Alfa Aesar), N-butyl trichlorosilane (Alfa Aesar).

TiO_2/FTO substrate: 2.5 cm x 7.5 cm FTO glass wafers were sonicated for 30 mins in a 25 vol% solution of Hellmanex in deionized water, followed by triplicate rinses in DI water (5 mins) and finally in 200 proof ethanol (1 min), also in the sonic bath. Prior to TiO_2 coating, the FTO substrates were UV-ozone treated to remove any residual organic matter and enhance the wettability of the substrate towards the titania paste. The commercial TiO_2 paste was then doctor bladed on the FTO substrate to form a film 5 - 10μm thick. The film was annealed at 160˚C for 30 mins and then calcined at 450˚C for 1 hour.

Note: The doctor blading process introduces thickness variation in the TiO_2 scaffold between samples as shown by the UV-Vis absorption data (Fig S4) and SEM cross-sectional images (Fig S5 a,c,e,g). This variation does not yield any variation in $CsPbI_3$ phase behavior, and thus scaffold thickness is not deemed a critical variable.

Silanization: A self-assembled monolayer of silane molecules was deposited on the sintered TiO_2/FTO substrates using a vapor assisted approach in a desiccator connected to a diaphragm pump. To facilitate the formation of hydroxyl groups on the TiO_2, the substrates were UV-ozone cleaned for 30 minutes prior to the silanization. A desiccator containing the substrates and a vial with 10 μL silane was exposed to dynamic vacuum for 1 minute and was then isolated and left at static vacuum for 1 hour to deposit a silane SAM on the substrates.

$CsPbI_3$ precursor solution and deposition: An equimolar precursor solution was prepared by dissolving 0.5 M cesium iodide and 0.5 M lead iodide in anhydrous N-methyl pyrrolidone (NMP) at room temperature inside a glove box under N_2 atmosphere. The precursor solution was then spin-coated on the TiO_2/FTO substrate at 3000 rpm for 2 mins. After the initial 5 secs, a constant N_2 flow was applied to the film for the entire duration of the spincoating process to rapidly dry off solvent and arrest crystallization in the pores. For all optical measurements freshly spincoated

$CsPbI_3$ on functionalized TiO_2 were enclosed inside lens tubes with quartz windows, sealed under the N_2 environment of a glovebox.

X-Ray Diffraction patterns (XRD): X-ray diffraction measurements for all samples were carried out in a Rigaku SmartLab X-ray diffractometer with a Cu anode which emitted a Kα wavelength of 0.154 nm. All the measurements were performed in open air at ambient temperature. No encapsulant was used on the samples.

Scanning Electron Microscopy (SEM): Surface morphology of the samples were characterized using scanning electron microscopy (SEM) images taken in a Zeiss Supra 50VP under high vacuum at a voltage of 3-5keV.

In situ UV-Vis: UV-Vis measurements were taken on a PerkinElmer LAMBDA 35 UV-Vis spectrophotometer. The sample cell was inserted into a VT Cell Variable Temperature Cell Holder (SPECAC LTD) to obtain the temperature dependent absorbance spectra. The temperature of the cell was increased from 25˚C to 80˚C at intervals of 5˚C over the course of 2 hours.

Photoluminescence studies: Steady-state photoluminescence (ssPL) and transient time-resolved photoluminescence (trPL) studies of $CsPbI_3$ deposited on functionalized TiO_2 surface were carried out on a FLS 1000 photoluminescent spectrometer (Edinburg Instruments). Steady state monochromatized light with an excitation wavelength of 530 nm and an integrating sphere were used to measure the ssPL emission spectra. Pulsed laser diode excitation of 650 nm and time-correlated single photon counting were used for trPL decays.

Results and Discussion

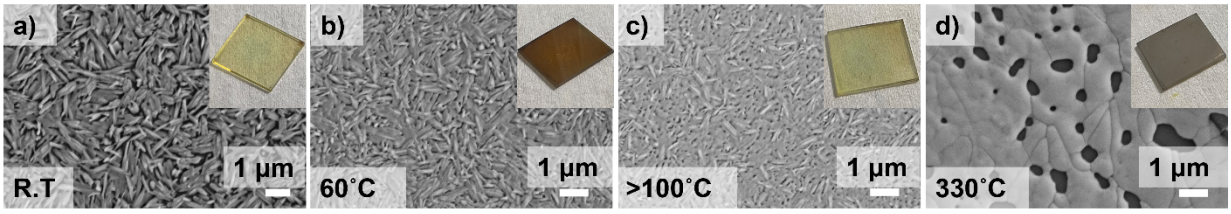

Figure 1: Phase behavior of $CsPbI_3$/NMP spincoated on glass with increasing annealing temperature. SEM images along with inset photos of 1 cm^2 samples, measured at room temperature after annealing to the indicated temperature for 10-15 min. **a)** Needle like crystals at room temperature for a yellow film, **b)** Needle like morphology largely maintained after heating to 60 ˚C while film transitions to brown color, **c)** Evidence of the beginning of grain consolidation by 120 ˚C, along with transition to a yellow film, **d)** Large consolidated domains at 330 ˚C corresponding with a metastable black film that reverts to yellow on exposure to air.

The various phases that form at different temperatures and degrees of desolvation can be distinguished from one another by their observed color, microscopic morphology and, most directly, by X-ray diffraction. Seeking to study the phase dynamics of the pure $CsPbI_3$ solid and not its various solvent-adducts, we chose to deposit thin films from the solvent N-methyl-2-pyrrolidone (NMP) for its relatively weak complex with lead.[33] On a simple, planar, glass substrate, i.e., in the absence of any confining scaffold, the phase sequence of thin-film $CsPbI_3$ exhibits a striking deviation from the single yellow-to-black equilibrium phase transition observed for bulk crystals described above. As observed in the inset photos of Fig 1(a-b), the $CsPbI_3$ is initially a translucent, pale yellow at room temperature and readily transitions to a translucent, deep brown by 60-70˚C, confirmed to be the perovskite phase by XRD (Fig S1). The morphology under these conditions, observed by SEM, consists of needle-shaped crystallites possessing one long axis and two shorter axes, the latter with dimensions on the sub-100 nm scale (Fig 1a). The shorter axes are

thus representative of the size regime where nanostructuring effects that favor the perovskite phase of $CsPbI_3$ are known to occur.[9–13,15,19] This nanostructure-induced stability is a spontaneous feature of this system, occurring without the addition of any extrinsic additives. Upon heating to higher temperatures however, the perovskite phase is revealed to be metastable, transforming back to the yellow non-perovskite phase at temperatures above 100˚C (Fig 1c inset and Fig S1). This would seem to contradict the premise that nanostructuring has thermodynamically favored the perovskite phase, however, examination of the morphology by SEM shows the onset of some consolidation (i.e., 'coarsening' or 'ripening') of the needle-like crystals into larger domains (Fig 1c). This black-to-yellow transition is *not* reversible—cooling below 100 ˚C does not recover the black phase. This is to be expected: consolidation is irreversible and will act to diminish any spontaneous nanostructuring effect, thus allowing the yellow phase to dominate, in accordance with the phase diagram in the bulk. For films annealed above 320˚C, the consolidation is rampant and only micron-scale domain boundaries are observed (Fig 1d). For such films, a (reversible) transition from yellow to black occurs near 320˚C, where it is expected based on the bulk phase diagram of $CsPbI_3$. The existence of the glass-perovskite interface has no significant impact on this phase transition temperature.

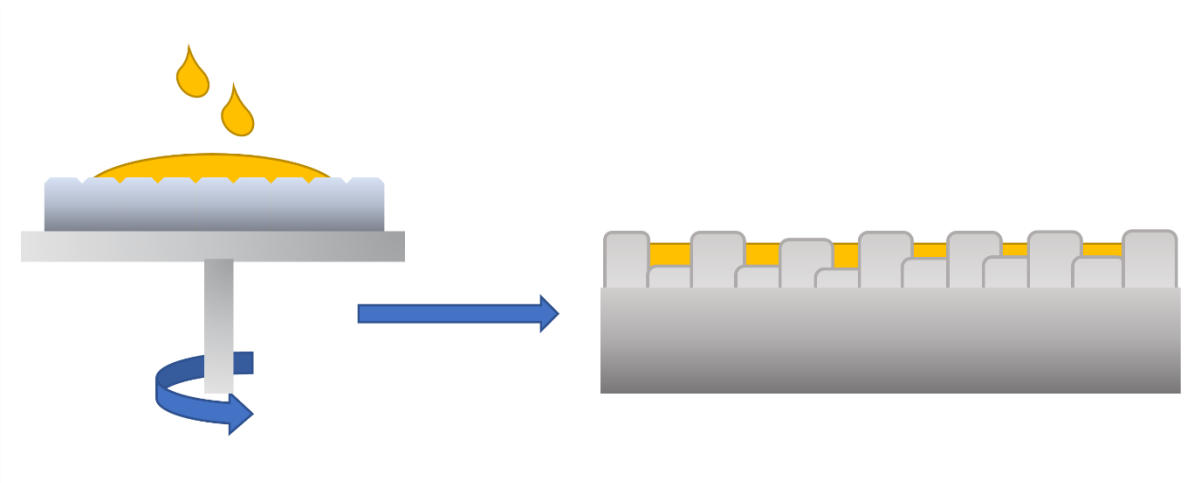

Scheme 1: Spincoating precursor solution on open TiO_2 scaffolds to infiltrate and crystallize $CsPbI_3$ in the voids.

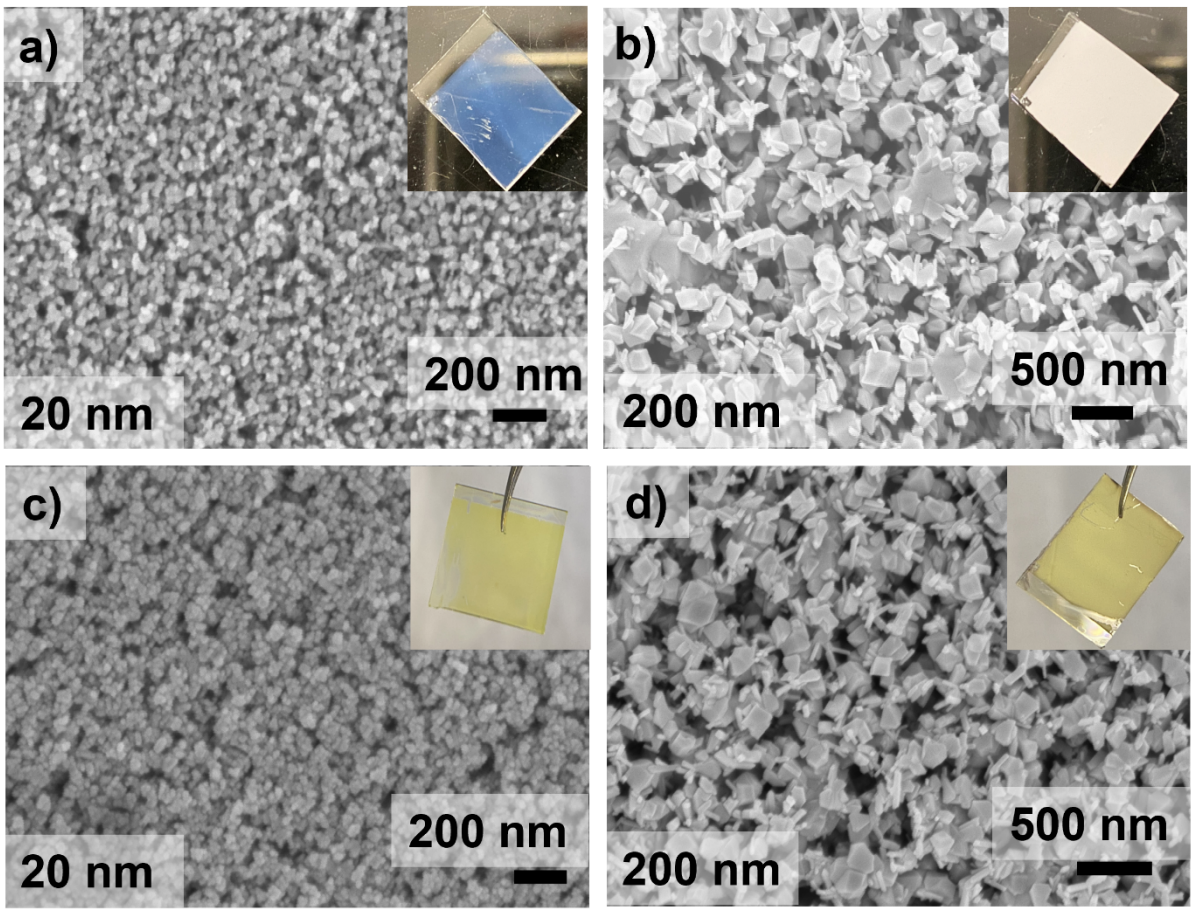

Figure 2: Empty and $CsPbI_3$-infiltrated TiO_2 scaffolds. SEM images showing **a)** 20 nm unfilled TiO_2 on FTO, **b)** 200 nm unfilled TiO_2 on FTO, **c)** 20 nm TiO_2 filled with $CsPbI_3$, **d)** 200 nm TiO_2 filled with $CsPbI_3$. Photos in inset shows 1 cm x 1 cm samples of unfilled TiO_2 and filled TiO_2.

To test the hypothesis that the minimum requirement for stabilization of the perovskite phase is disruption of long-range crystalline order, we deposited $CsPbI_3$ on to high-surface-area nano- and meso-porous TiO_2 scaffolds according to Scheme 1. The scaffolds were created by blade-coating and subsequent calcination of titania pastes of either 20 or 200 nm particle size on FTO coated glass substrates, as shown in Fig 2(a-b). The scaffolds maintain their crystalline grain size and open, porous structure though the calcining process as corroborated by SEM (Fig 2a-b), Scherrer analysis of the XRD pattern (Fig S2), and by the relative opacity due to light scattering by the voids, evident in the inset photos in Fig 2(a-b). Automated pore size distribution analysis of the open surface is presented in Fig S3. To avoid pooling of the precursor on the top of the scaffold and to ensure adequate infiltration of the pores, the $CsPbI_3$ precursor solution was spincoated on the TiO_2 scaffolds according to Scheme 1. The $CsPbI_3$ coats but does not completely fill the voids of the scaffold and no bulk material is observed outside the scaffold, as seen by SEM in the Fig 2(c-d) and cross-sections in Fig S5.

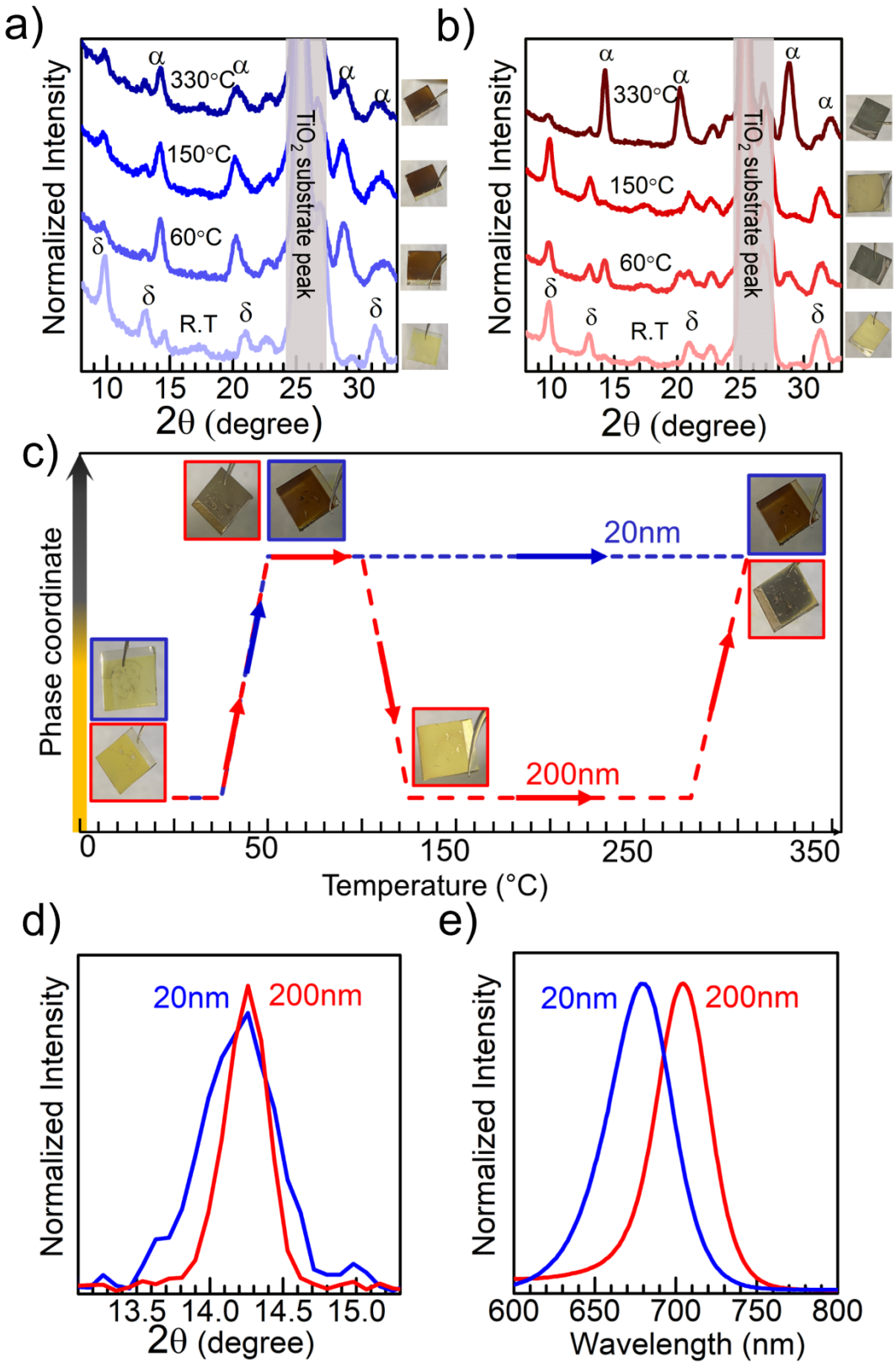
a)
b)
Normalized Intensity
330°C
150°C
60°C
R.T
α
δ
TiO2 substrate peak
10 15 20 25 30
2θ (degree)
c)
Phase coordinate
20nm
200nm
0 50 150 250 350
Temperature (°C)
d)
e)
Normalized Intensity
20nm
200nm
13.5 14.0 14.5 15.0
2θ (degree)
600 650 700 750 800
Wavelength (nm)

Figure 3: Phase and photoluminescence behavior of $CsPbI_3$ in 20 nm (blue) or 200 nm (red) scaffolds. **a-b)** XRD showing the sequence of phase transitions with increasing annealing temperature when $CsPbI_3$ is embedded in a 20 nm or 200 nm TiO_2 scaffold, respectively. **c)** Schematic showing the phase transition sequence of $CsPbI_3$ in the 20 nm vs 200 nm TiO_2 scaffold as a function of annealing temperature. The y-axis represents the transition between the yellow and black phases of $CsPbI_3$ in 20 nm and 200 nm TiO_2 scaffolds. All photos in inset (a-c) are of 1 cm^2 samples at room temperature after annealing to the indicated temperature for 10-15 min. **d)** Comparison of peak width for 001 perovskite peak in 20 nm vs 200 nm TiO_2 scaffold as a measure of Scherrer [i.e., grain-size-dependent] broadening. **e)** Scaffold-size dependent PL emission response of $CsPbI_3$. All measurements made at room temperature after annealing to the indicated temperature, which for (d-e) was 100 °C.

To compare with the behavior of the non-scaffolded thin films of Fig 1, the phase of scaffold-supported $CsPbI_3$ as a function of annealing temperature was studied by XRD, shown in Fig 3(a-b); in all cases, XRD corroborates what can be seen by eye based on the color (photo insets). To summarize, for the 20 nm scaffold, the phase behavior with annealing diverges significantly from non-scaffolded films; in contrast, 200 nm scaffolds behave identically to non-scaffolded films. The detailed observations are as follows. Whether scaffolded or not, all examples begin as the yellow, non-perovskite, *Pnma* orthorhombic, δ-phase $CsPbI_3$ after spin-coating at room temperature, with diagnostic peaks at 9.95, 13 and 20.99 degrees 2θ positions. In all cases, as the temperature approaches approximately 60 °C, the color evolves to brown; XRD measurements, taken after cooling back to room temperature, show prominent reflexes characteristic of the perovskite phase of $CsPbI_3$ at 14.25, 20.5, 28.5 2θ in Fig 3(a-b) corresponding to the 001, 111, 002 planes respectively of the cubic *Pm3m* structure. (Note that the peak indexing of the parent, high symmetry, cubic phase is used throughout, however it is likely that the lower symmetry, distorted cubic perovskite phases known to this material are present but difficult to resolve due to peak

broadening.[8]) Like non-scaffolded films, the perovskite phase in a 200 nm scaffold is highly unstable at room temperature: either increasing the temperature or exposure to atmospheric humidity causes this perovskite phase to revert to yellow in minutes. Only above the bulk phase transition temperature of 320 °C can the perovskite phase be recovered. In contrast, in the 20 nm scaffold, the perovskite phase remains stable at all temperatures, from the initial phase transition in the range of 60-70 °C up to and beyond 320 °C. In other words, $CsPbI_3$ on the smaller, 20 nm nanocrystal scaffold exhibits a *durable* nanostructuring effect (improvement of perovskite phase stability by 250 °C), whereas on 200 nm scaffolds, it behaves identically to unstructured films, namely, it exhibits a transitory stabilization effect due to nanosized grains which subsequently coarsen. This phase transition sequence is depicted in Fig 3c.

In order to establish the minimum size range of crystalline order present in the scaffolded $CsPbI_3$, Scherrer analysis was applied to the peak width of the 001 reflex. The FWHMs for the perovskite in 20 nm and 200 nm scaffolds were found to be 0.59 and 0.35 respectively as shown in Fig 3d, corresponding to a minimum mean size of crystalline ordered domains of 15 and 26 nm, respectively. Inhomogeneous strain and instrumental broadening also contribute to the FWHM therefore this difference indicates only a likely *relative* decrease in long-range crystalline order for the 20 nm scaffold. Steady-state photoluminescence of the perovskite phase $CsPbI_3$ corroborated a scaffold-size-dependent perturbation of the structure consistent with reduced crystallite size[15,34] in the 20 nm case: a 15 nm blue shift was observed in the emission peak in 20 nm scaffold (690 nm), relative to the bulk-like $CsPbI_3$ peak at 705 nm in the 200 nm scaffold as shown in Fig 3e. The similar linewidth of the emission is also indicative of a similar degree of electronic disorder and hence structural disorder, supporting the interpretation of the XRD linewidth as predominantly size and not strain-related. XRD and photoluminescence indicate that the primary impact of the

smaller pore-size scaffold is to limit the crystal grain size, thus it is suggestive that the resulting short-range crystal order is the critical attribute of scaffolded $CsPbI_3$ that enables a low temperature perovskite phase.

DFT calculations that have rationalized the nanostructuring effect have specifically calculated a threshold surface-to-volume ratio at which a favorable ΔE_{surf} renders the perovskite stable; hypothetically this ratio could be achieved quite simply by making an extremely thin, uniform film. Possessing equivalent surface-to-volume ratio, a stable cube with dimensions of 100 nm[13] or less corresponds with a thin film being stable at approximately 30 nm or thinner. We know of no examples of $CsPbI_3$ films as thin as this, and our own attempts to fabricate them via spincoating instead resulted in discreet islands of crystals when the average film thickness is below 100 nm, leaving this particular prediction untested.

However, we can shed further light on how ΔE_{surf} does or does not depend on the interface. Smaller pore size also corresponds to greater surface area, which creates greater opportunity for ΔE_{surf} to be influenced by interfacial strain or specific chemical interactions with the interface.

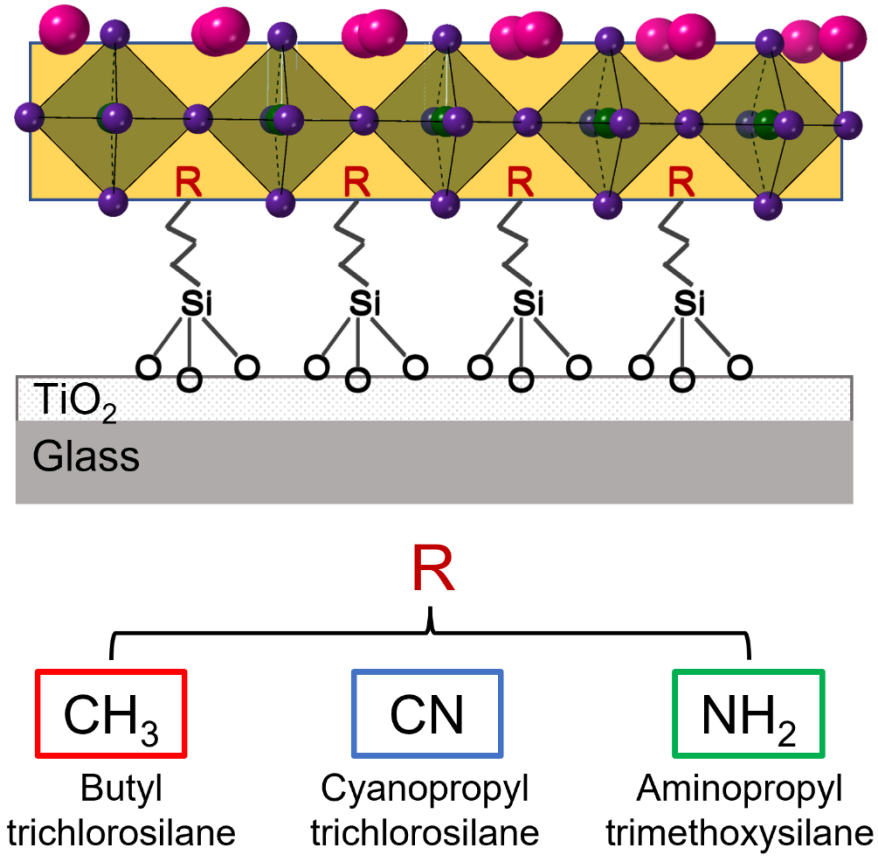

Figure 4. Schematic showing a silane modified interface between the TiO_2 and $CsPbI_3$.

To differentiate the contributions of size and interfacial interactions to the dramatic phase stabilization achieved by the 20 nm scaffold, we modulated the interface between the perovskite and the scaffold by modifying the TiO_2 surface with functionalized alkylsilanes prior to infilling with perovskite, as in the schematic in Fig 4. In this manner, in addition to bare TiO_2, the surface was capped with a $–(CH_2)_3–$ hydrocarbon chain, terminated with either an amine ($-NH_2$) group, a nitrile group (-CN) or a methyl group ($-CH_3$), to form an ionizable, a polar and a non-polar interface, respectively. Water contact angle tests (Fig S6) and FTIR studies (Fig S7) were

performed on the silane modified TiO_2 surfaces to confirm the presence of the specific chemical groups on the TiO_2 surface.

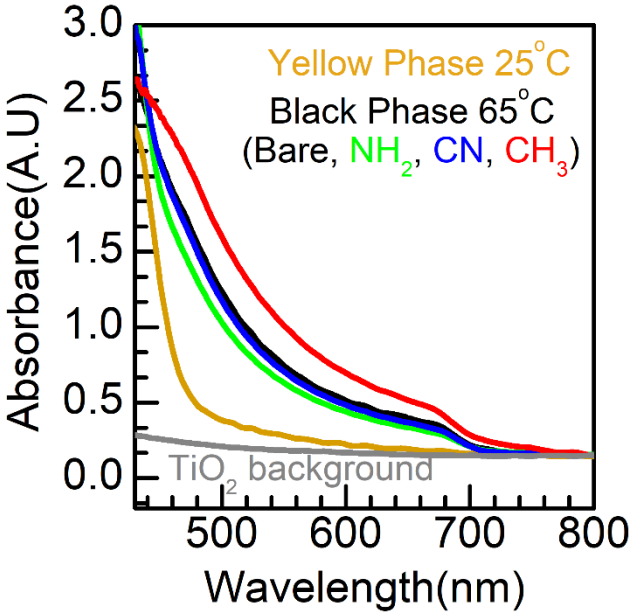

Figure 5: In-situ UV-Vis measurements showing yellow-to-black phase transition at 65 ˚C for $CsPbI_3$ on bare and modified 20 nm TiO_2 surfaces.

We performed temperature-dependent *in-situ* UV-Vis measurements to determine the phase transition temperature of $CsPbI_3$ on TiO_2 with this set of chemical terminations. Fig 5 shows the temperature-dependent absorbance spectra for $CsPbI_3$ on all the silane-modified TiO_2 surfaces. Regardless of interfacial surface chemistry, these measurements showed essentially no differences: a consistent low yellow-to-black phase transition temperature occurring between 60-70 ˚C is always observed. Thus, we conclude that the chemical identity of the scaffold surface has little impact on ΔE_{surf}.

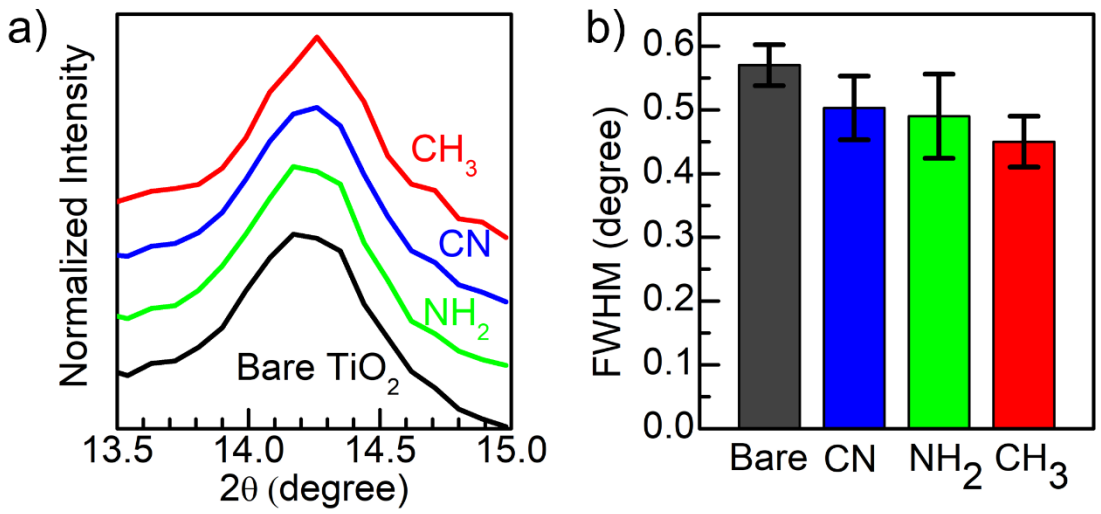

Figure 6: Effect of modified surface energy on grain size. **a)** XRD showing 001 perovskite peak for $CsPbI_3$ on modified TiO_2 surfaces. **b)** Average FWHM for 14.2-degree 2θ peak. A broad peak was observed for $CsPbI_3$ deposited on all three kinds of functionalized TiO_2 substrates.

The position and FWHM of the 001 reflex of scaffolded $CsPbI_3$ is similar across all surface treatments as shown by XRD in Fig 6a and 6b respectively, indicating that they do not impact the ability of the perovskite precursor solution to penetrate or crystalize within the scaffold pores; specifically, there is no dramatic narrowing that might indicate unconstrained crystallization outside the pores. However, there is a very slight difference in FWHM (significant within a 90% confidence interval) between bare and CH_3–terminated surfaces that could be either due to Scherrer- or strain-dependent-broadening. If the latter, it would indicate the greatest strain in the bare case, as might be expected for a rigid inorganic scaffold interface as compared to that formed from the various organic monolayers. This is suggestive that even in the likely presence of scaffold-induced lattice strain (in the bare case), the value of ΔE_{surf} is insufficiently perturbed to manifest in an observable shift in phase transition temperature, further emphasizing that

nanostructuring effects on crystal phase stability emerge primarily from intrinsic, rather than substrate-mediated forces.

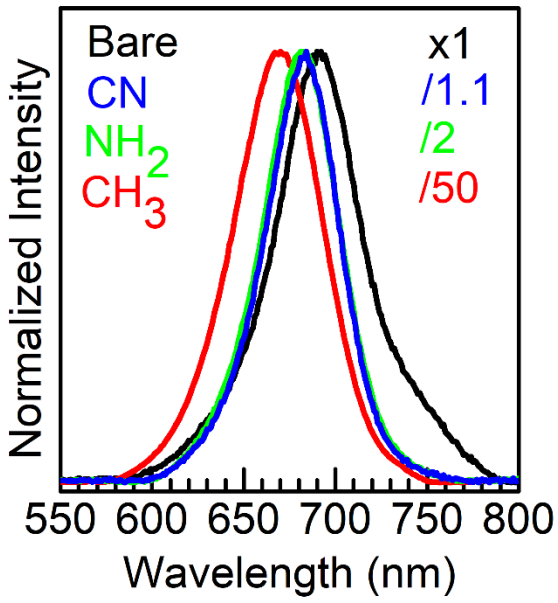

Figure 7: Effect of modified surface chemistry on photoluminescence. Steady state photoluminescence data using an integrating sphere showing surface dependent shift in emission peak of $CsPbI_3$ deposited on surface modified TiO_2 surfaces. Relative normalization factor of photoluminescence intensity shown as legend on the right-hand side.

Despite no measurable impact on phase transition temperature, there are electronic differences as a consequence of interface modification, as observed in the photoluminescence behavior. In Fig 7, the $CsPbI_3$ emission peak shifts to higher energy for the surface modified TiO_2, to a different degree for each interface. The emission peaks on bare, NH_2-, CN- and CH_3-terminated TiO_2 are 690 nm, 683 nm, 684 nm, and 670 nm, respectively. Blue shifts of the photoluminescence emission as a consequence of the inclusion of organic monolayers at a perovskite/electron-transport layer interface are well documented.[35–37] The blue shift has been attributed to a reduction in energetic disorder at the interface, leading to an expansion of the effective band gap[36,37] (i.e. a reduction in

band tailing[38]) due to passivation of dangling bonds at the oxide surface; we speculate that the same effect is occurring in the present case. Of the three SAMs, CH_3-termination at the interface exhibits both the largest blue-shift with respect to bare TiO_2 and the narrowest diffraction peak, as noted above, consistent with the hypothesis that the perovskite/CH_3-interface exhibits negligible interfacial strain, which manifests both as minimal energetic disorder and the least structural heterogeneity.

Separately, we note 25-50 times higher photoluminescence intensity for $CsPbI_3$ deposited on butyl terminated TiO_2 as compared to that on bare, amine or nitrile terminated TiO_2 (relative normalization factors are shown in the right-hand legend of Fig 7 or Fig S8 shows absolute photoluminescence intensities). The increases in quantum yield are accompanied by slower quenching, observed by time-resolved photoluminescence studies (Fig S9); both changes are consistent with reduction in the charge injection kinetics from $CsPbI_3$ to the TiO_2 due to the modification of the work function of the oxide by the SAM, as seen in other studies,[35–37,39] or possibly changes in band alignment due to reduced band tailing. Alternatively, researchers have shown a relation between interfacial strain and charge injection kinetics,[40–42] though we doubt that the strain in $CsPbI_3$ is significantly different across the three SAM-modified scaffolds, given their similar XRD linewidths.

Our results have direct relevance to recent studies. Kong *et. al.* also observed perovskite-phase $CsPbI_3$ forming at low temperature (as low as ~100 ˚C) when confined in 250 nm diameter porous anodized alumina.[21] That study examined the solution-to-solid phase transition (termed as the 'wet-annealing' process) in contrast to the solid-state, delta-to-perovskite phase transition observed in the present work. The distinction allows us to exclude an alternative hypothesis to explain the observations of the prior study: the perovskite phase is the first solid to precipitate from solution,

after which the solid phase is kinetically trapped. Such trapping could occur due to the rigid confinement of the anodized alumina pores not allowing for the volume expansion required for a subsequent solid-state, equilibrium, phase transition. In the comparatively more open scaffolds of the present study, no 'wet-anneal' is required to produce the perovskite phase and we can directly observe the solid-state delta-to-perovskite phase transition. Therefore, it can now be more confidently asserted that the 'null effect' of scaffold surface chemistry is indeed towards the thermodynamic quantity, ΔE_{surf} rather than towards the kinetics of precipitation. Additionally, our study shows that the null effect persists down to smaller crystallite sizes and even more depressed phase transition temperatures and that strain is not critical to the nanosize effect.

Conclusion

Nanoscaffolding is increasingly appreciated as a robust approach to stabilizing the perovskite phase of $CsPbI_3$. Employing an easily fabricated scaffold composed of TiO_2 nanoparticles, we have shown a depression of the apparent delta-to-perovskite phase transition of $CsPbI_3$ to temperatures as low as 60-70 ˚C. Previous approaches have included confining the perovskite in the pores of anodized aluminum oxide or, in the case of colloidal nanocrystals, encasing it within a ligand shell. Rather than confining the crystal, in this case, the scaffold is open, and its tortuosity alone prevents the development of long-range crystalline order. Thus, we have identified the simplest substantiation of the nanoscaffolding effect: holding the surface chemistry constant and varying only the pore size, we observe that limiting long-range crystalline order below 10^2 nm is all that is required to favor the perovskite phase.

We probed the extent to which interfacial energetics impact the phase transition thermodynamics in the 20 nm TiO_2 scaffold by systematically functionalizing the surface of the scaffold. The strong and chemically specific influence of the various SAMs on the perovskite's photophysics is strong

evidence of significantly modified chemical interactions at the interface, nonetheless, the temperature of the onset of the perovskite phase is constant across all interfaces studied. The observed null-effect on phase transition temperature encompasses surfaces spanning a wide range of surface tensions and include interfaces that have been shown previously to support strong substrate-induced strain (bare) and those less capable of doing so (e.g. -CH_3 termination). This further reinforces the conclusion that the large observed depression of the phase transition temperature is due to internal forces within the perovskite, and independent of extrinsic interfacial forces. In other words, ΔE_{surf} must be dominated by the intrinsic electrostatic and quantum mechanical consequences of interrupting the $CsPbI_3$ crystal lattice. The approach to nanostructuring employed here is highly general and could be applied to a variety of crystalline materials with covalent and ionic binding character for which the lower density phase is more desirable.

ASSOCIATED CONTENT

Supporting Information: XRD data of $CsPbI_3$ thin film phase transition on glass substrates; Detailed characterization of 20 nm and 200 nm TiO_2 showing Scherrer broadening in XRD peaks, variations in scaffold thickness and pore size distribution; cross-sectional SEM of filled and unfilled 20 and 200nm TiO_2 scaffolds; water contact angle photographs and FTIR spectra of surface modified 20nm TiO_2 scaffolds; steady-state and time-resolved photoluminescence data for $CsPbI_3$ in surface modified scaffolds.

AUTHOR INFORMATION

Corresponding Author

Email: fafarman@drexel.edu

ORCID ID:

Aaron T. Fafarman: 0000-0003-3652-3383

Arkita Chakrabarti: 0000-0002-6597-3503

Benjamin M. Lefler: 0000-0003-0205-8479

Present Addresses

†B.M.L: Department of Material Science and Engineering, North Carolina State University, Raleigh, NC, 27695, USA

Author Contributions

The manuscript was written through contributions of all authors. All authors have given approval to the final version of the manuscript.

Funding Sources

National Science Foundation CAREER Award DMR# 1847952.

Notes

The authors declare no competing financial interests.

ACKNOWLEDGMENT

A.C. and A.T.F. were supported by the National Science Foundation CAREER Award DMR# 1847952. SEM, and XRD analyses were performed using instruments in the Materials Characterization Core at Drexel University. Steady-state and time-resolved photoluminescence

measurements were performed in Prof. Cherie Kagan's lab at The University of Pennsylvania. The authors thank Subham Dastidar, Yaser Kashcooli and Jacob Bolduc for assistance with preliminary experiments.

REFERENCES

(1) Eperon, G. E.; Paternò, G. M.; Sutton, R. J.; Zampetti, A.; Haghighirad, A. A.; Cacialli, F.; Snaith, H. J. Inorganic Caesium Lead Iodide Perovskite Solar Cells. *J. Mater. Chem. A* **2015**, *3* (39), 19688–19695. https://doi.org/10.1039/C5TA06398A.

(2) Chang, X.; Fang, J.; Fan, Y.; Luo, T.; Su, H.; Zhang, Y.; Lu, J.; Tsetseris, L.; Anthopoulos, T. D.; Liu, S. (Frank); et al. Printable CsPbI3 Perovskite Solar Cells with PCE of 19% via an Additive Strategy. *Advanced Materials* **2020**, *32* (40), 2001243. https://doi.org/10.1002/adma.202001243.

(3) Trots, D. M.; Myagkota, S. V. High-Temperature Structural Evolution of Caesium and Rubidium Triiodoplumbates. *Journal of Physics and Chemistry of Solids* **2008**, *69* (10), 2520–2526. https://doi.org/10.1016/j.jpcs.2008.05.007.

(4) Dastidar, S.; Hawley, C. J.; Dillon, A. D.; Gutierrez-Perez, A. D.; Spanier, J. E.; Fafarman, A. T. Quantitative Phase-Change Thermodynamics and Metastability of Perovskite-Phase Cesium Lead Iodide. *J. Phys. Chem. Lett.* **2017**, *8* (6), 1278–1282. https://doi.org/10.1021/acs.jpclett.7b00134.

(5) Wang, B.; Novendra, N.; Navrotsky, A. Energetics, Structures, and Phase Transitions of Cubic and Orthorhombic Cesium Lead Iodide ($CsPbI_3$) Polymorphs. *J. Am. Chem. Soc.* **2019**, *141* (37), 14501–14504. https://doi.org/10.1021/jacs.9b05924.

(6) Steele, J. A.; Jin, H.; Dovgaliuk, I.; Berger, R. F.; Braeckevelt, T.; Yuan, H.; Martin, C.; Solano, E.; Lejaeghere, K.; Rogge, S. M. J.; et al. Thermal Unequilibrium of Strained Black CsPbI $_3$ Thin Films. *Science* **2019**, *365* (6454), 679–684. https://doi.org/10.1126/science.aax3878.

(7) Marronnier, A.; Roma, G.; Boyer-Richard, S.; Pedesseau, L.; Jancu, J.-M.; Bonnassieux, Y.; Katan, C.; Stoumpos, C. C.; Kanatzidis, M. G.; Even, J. Anharmonicity and Disorder in the Black Phases of Cesium Lead Iodide Used for Stable Inorganic Perovskite Solar Cells. *ACS Nano* **2018**, *12* (4), 3477–3486. https://doi.org/10.1021/acsnano.8b00267.

(8) Sutton, R. J.; Filip, M. R.; Haghighirad, A. A.; Sakai, N.; Wenger, B.; Giustino, F.; Snaith, H. J. Cubic or Orthorhombic? Revealing the Crystal Structure of Metastable Black-Phase CsPbI $_3$ by Theory and Experiment. *ACS Energy Lett.* **2018**, *3* (8), 1787–1794. https://doi.org/10.1021/acsenergylett.8b00672.

(9) Wang, Y.; Zhang, T.; Kan, M.; Zhao, Y. Bifunctional Stabilization of All-Inorganic α-CsPbI $_3$ Perovskite for 17% Efficiency Photovoltaics. *J. Am. Chem. Soc.* **2018**, *140* (39), 12345–12348. https://doi.org/10.1021/jacs.8b07927.

(10) Wang, Q.; Zheng, X.; Deng, Y.; Zhao, J.; Chen, Z.; Huang, J. Stabilizing the α-Phase of CsPbI3 Perovskite by Sulfobetaine Zwitterions in One-Step Spin-Coating Films. *Joule* **2017**, *1* (2), 371–382. https://doi.org/10.1016/j.joule.2017.07.017.

(11) Huang, Y.; Luan, W.; Liu, M.; Turyanska, L. DDAB-Assisted Synthesis of Iodine-Rich CsPbI $_3$ Perovskite Nanocrystals with Improved Stability in Multiple Environments. *J. Mater. Chem. C* **2020**, *8* (7), 2381–2387. https://doi.org/10.1039/C9TC06566K.

(12) Wang, Y.; Dar, M. I.; Ono, L. K.; Zhang, T.; Kan, M.; Li, Y.; Zhang, L.; Wang, X.; Yang, Y.; Gao, X.; et al. Thermodynamically Stabilized β-CsPbI3–Based Perovskite Solar Cells with Efficiencies >18%. *Science* **2019**, *365* (6453), 591–595. https://doi.org/10.1126/science.aav8680.

(13) Zhao, B.; Jin, S.-F.; Huang, S.; Liu, N.; Ma, J.-Y.; Xue, D.-J.; Han, Q.; Ding, J.; Ge, Q.-Q.; Feng, Y.; et al. Thermodynamically Stable Orthorhombic γ-$CsPbI_3$ Thin Films for High-Performance Photovoltaics. *J. Am. Chem. Soc.* **2018**, *140* (37), 11716–11725. https://doi.org/10.1021/jacs.8b06050.

(14) Zhang, Y.; Yang, Y.; Zhang, X.; Wang, T.; Nian, L.; Rong, Q.; Zhou, G.; Li, N. Low Temperature Preparation of All-Inorganic CsPbI3 Perovskite Solar Cells with Ethanediamine as Additive. *Organic Electronics* **2020**, *87*, 105940. https://doi.org/10.1016/j.orgel.2020.105940.

(15) Protesescu, L.; Yakunin, S.; Bodnarchuk, M. I.; Krieg, F.; Caputo, R.; Hendon, C. H.; Yang, R. X.; Walsh, A.; Kovalenko, M. V. Nanocrystals of Cesium Lead Halide Perovskites ($CsPbX_3$, X = Cl, Br, and I): Novel Optoelectronic Materials Showing Bright Emission with Wide Color Gamut. *Nano Lett.* **2015**, *15* (6), 3692–3696. https://doi.org/10.1021/nl5048779.

(16) Zhao, Q.; Hazarika, A.; Schelhas, L. T.; Liu, J.; Gaulding, E. A.; Li, G.; Zhang, M.; Toney, M. F.; Sercel, P. C.; Luther, J. M. Size-Dependent Lattice Structure and Confinement Properties in $CsPbI_3$ Perovskite Nanocrystals: Negative Surface Energy for Stabilization. *ACS Energy Lett.* **2020**, *5* (1), 238–247. https://doi.org/10.1021/acsenergylett.9b02395.

(17) Huang, H.; Li, Y.; Tong, Y.; Yao, E.-P.; Feil, M. W.; Richter, A. F.; Döblinger, M.; Rogach, A. L.; Feldmann, J.; Polavarapu, L. Spontaneous Crystallization of Perovskite Nanocrystals in Nonpolar Organic Solvents: A Versatile Approach for Their Shape-Controlled

Synthesis. *Angewandte Chemie International Edition* **2019**, *58* (46), 16558–16562. https://doi.org/10.1002/anie.201906862.

(18) Sun, S.; Yuan, D.; Xu, Y.; Wang, A.; Deng, Z. Ligand-Mediated Synthesis of Shape-Controlled Cesium Lead Halide Perovskite Nanocrystals via Reprecipitation Process at Room Temperature. *ACS Nano* **2016**, *10* (3), 3648–3657. https://doi.org/10.1021/acsnano.5b08193.

(19) Ma, S.; Kim, S. H.; Jeong, B.; Kwon, H.-C.; Yun, S.-C.; Jang, G.; Yang, H.; Park, C.; Lee, D.; et al. Strain-Mediated Phase Stabilization: A New Strategy for Ultrastable α-CsPbI3 Perovskite by Nanoconfined Growth. *Small* **2019**, *15* (21), 1900219. https://doi.org/10.1002/smll.201900219.

(20) Waleed, A.; Tavakoli, M. M.; Gu, L.; Hussain, S.; Zhang, D.; Poddar, S.; Wang, Z.; Zhang, R.; Fan, Z. All Inorganic Cesium Lead Iodide Perovskite Nanowires with Stabilized Cubic Phase at Room Temperature and Nanowire Array-Based Photodetectors. *Nano Lett.* **2017**, *17* (8), 4951–4957. https://doi.org/10.1021/acs.nanolett.7b02101.

(21) Kong, X.; Shayan, K.; Hua, S.; Strauf, S.; Lee, S. S. Complete Suppression of Detrimental Polymorph Transitions in All-Inorganic Perovskites via Nanoconfinement. *ACS Appl. Energy Mater.* **2019**, *2* (4), 2948–2955. https://doi.org/10.1021/acsaem.9b00322.

(22) Romero-Pérez, C.; Rubino, A.; Caliò, L.; Calvo, M. E.; Míguez, H. Optoelectronic Devices Based on Scaffold Stabilized Black-Phase CsPbI3 Nanocrystals. *Advanced Optical Materials* **2022**, *10* (6), 2102112. https://doi.org/10.1002/adom.202102112.

(23) Becker, P.; Márquez, J. A.; Just, J.; Al-Ashouri, A.; Hages, C.; Hempel, H.; Jošt, M.; Albrecht, S.; Frahm, R.; Unold, T. Low Temperature Synthesis of Stable γ-CsPbI3 Perovskite

Layers for Solar Cells Obtained by High Throughput Experimentation. *Advanced Energy Materials* **2019**, *9* (22), 1900555. https://doi.org/10.1002/aenm.201900555.

(24) Dastidar, S.; Egger, D. A.; Tan, L. Z.; Cromer, S. B.; Dillon, A. D.; Liu, S.; Kronik, L.; Rappe, A. M.; Fafarman, A. T. High Chloride Doping Levels Stabilize the Perovskite Phase of Cesium Lead Iodide. *Nano Lett.* **2016**, *16* (6), 3563–3570. https://doi.org/10.1021/acs.nanolett.6b00635.

(25) Kong, X.; Zong, K.; Lee, S. S. Nanoconfining Optoelectronic Materials for Enhanced Performance and Stability. *Chem. Mater.* **2019**, *31* (14), 4953–4970. https://doi.org/10.1021/acs.chemmater.9b01707.

(26) Masi, S.; Gualdrón-Reyes, A. F.; Mora-Seró, I. Stabilization of Black Perovskite Phase in FAPbI3 and CsPbI3. *ACS Energy Lett.* **2020**, *5* (6), 1974–1985. https://doi.org/10.1021/acsenergylett.0c00801.

(27) Ayyub, P.; Palkar, V. R.; Chattopadhyay, S.; Multani, M. Effect of Crystal Size Reduction on Lattice Symmetry and Cooperative Properties. *Physical Review B* **1995**, *51* (9), 6135–6138. https://doi.org/10.1103/PhysRevB.51.6135.

(28) Gamarnik, M. Ya. Size Changes of Lattice Parameters in Ultradisperse Diamond and Silicon. *physica status solidi (b)* **1990**, *161* (2), 457–462. https://doi.org/10.1002/pssb.2221610202.

(29) Ya Gamarnik, M. The Physical Nature of Changes of Lattice Parameters in Small Particles. *physica status solidi (b)* **1993**, *178* (1), 59–69. https://doi.org/10.1002/pssb.2221780105.

(30) Yang, R. X.; Tan, L. Z. Understanding Size Dependence of Phase Stability and Band Gap in $CsPbI_3$ Perovskite Nanocrystals. *J. Chem. Phys.* **2020**, *152* (3), 034702. https://doi.org/10.1063/1.5128016.

(31) Fu, Y.; Rea, M. T.; Chen, J.; Morrow, D. J.; Hautzinger, M. P.; Zhao, Y.; Pan, D.; Manger, L. H.; Wright, J. C.; Goldsmith, R. H.; et al. Selective Stabilization and Photophysical Properties of Metastable Perovskite Polymorphs of CsPbI3 in Thin Films. *Chem. Mater.* **2017**, *29* (19), 8385–8394. https://doi.org/10.1021/acs.chemmater.7b02948.

(32) Grosso, D.; Soler-Illia, G. J. de A. A.; Crepaldi, Eduardo. L.; Cagnol, F.; Sinturel, C.; Bourgeois, A.; Brunet-Bruneau, A.; Amenitsch, H.; Albouy, P. A.; et al. Highly Porous TiO2 Anatase Optical Thin Films with Cubic Mesostructure Stabilized at 700 °C. *Chem. Mater.* **2003**, *15* (24), 4562–4570. https://doi.org/10.1021/cm031060h.

(33) Stevenson, J.; Sorenson, B.; Subramaniam, V. H.; Raiford, J.; Khlyabich, P. P.; Loo, Y.-L.; Clancy, P. Mayer Bond Order as a Metric of Complexation Effectiveness in Lead Halide Perovskite Solutions. *Chem. Mater.* **2017**, *29* (6), 2435–2444. https://doi.org/10.1021/acs.chemmater.6b04327.

(34) Swarnkar, A.; Marshall, A. R.; Sanehira, E. M.; Chernomordik, B. D.; Moore, D. T.; Christians, J. A.; Chakrabarti, T.; Luther, J. M. Quantum Dot-Induced Phase Stabilization of Alpha-CsPbI3 Perovskite for High-Efficiency Photovoltaics. *Science* **2016**, *354* (6308), 92–95. https://doi.org/10.1126/science.aag2700.

(35) Zuo, L.; Gu, Z.; Ye, T.; Fu, W.; Wu, G.; Li, H.; Chen, H. Enhanced Photovoltaic Performance of CH3NH3PbI3 Perovskite Solar Cells through Interfacial Engineering Using Self-

Assembling Monolayer. *J. Am. Chem. Soc.* **2015**, *137* (7), 2674–2679. https://doi.org/10.1021/ja512518r.

(36) Yang, G.; Wang, C.; Lei, H.; Zheng, X.; Qin, P.; Xiong, L.; Zhao, X.; Yan, Y.; Fang, G. Interface Engineering in Planar Perovskite Solar Cells: Energy Level Alignment, Perovskite Morphology Control and High Performance Achievement. *J. Mater. Chem. A* **2017**, *5* (4), 1658–1666. https://doi.org/10.1039/C6TA08783C.

(37) Shao, Y.; Xiao, Z.; Bi, C.; Yuan, Y.; Huang, J. Origin and Elimination of Photocurrent Hysteresis by Fullerene Passivation in CH3NH3PbI3 Planar Heterojunction Solar Cells. *Nat Commun* **2014**, *5* (1), 5784. https://doi.org/10.1038/ncomms6784.

(38) Wright, A. D.; Milot, R. L.; Eperon, G. E.; Snaith, H. J.; Johnston, M. B.; Herz, L. M. Band-Tail Recombination in Hybrid Lead Iodide Perovskite. *Advanced Functional Materials* **2017**, *27* (29), 1700860. https://doi.org/10.1002/adfm.201700860.

(39) Zuo, L.; Chen, Q.; De Marco, N.; Hsieh, Y.-T.; Chen, H.; Sun, P.; Chang, S.-Y.; Zhao, H.; Dong, S.; Yang, Y. Tailoring the Interfacial Chemical Interaction for High-Efficiency Perovskite Solar Cells. *Nano Lett.* **2017**, *17* (1), 269–275. https://doi.org/10.1021/acs.nanolett.6b04015.

(40) Zhu, C.; Niu, X.; Fu, Y.; Li, N.; Hu, C.; Chen, Y.; He, X.; Na, G.; Liu, P.; Zai, H.; et al.. Strain Engineering in Perovskite Solar Cells and Its Impacts on Carrier Dynamics. *Nat Commun* **2019**, *10* (1), 815. https://doi.org/10.1038/s41467-019-08507-4.

(41) Yu, H.; Sun, Q.; Zhang, T.; Zhang, X.; Shen, Y.; Wang, M. Is the Strain Responsible to Instability of Inorganic Perovskites and Their Photovoltaic Devices? *Materials Today Energy* **2021**, *19*, 100601. https://doi.org/10.1016/j.mtener.2020.100601.

(42) Cao, Y.-H.; Li, Y.-F.; He, J.-W.; Qian, C.-X.; Zhang, Q.; Bai, J.-T.; Feng, H.-J. Asymmetric Strain-Introduced Interface Effect on the Electronic and Optical Properties of the CsPbI3/SnS van Der Waals Heterostructure. *Advanced Materials Interfaces* **2019**, *6* (24), 1901330. https://doi.org/10.1002/admi.201901330.

TOC Graphic